Proceedings of The First International Conference on Vortex Methods, November 4-5, 1999, Kobe, Japan

VORTEX METHOD ANALYSIS OF TURBULENT FLOWS

Peter S. Bernard
Department of Mechanical Engineering, University of Maryland
College Park, Maryland, 20742 / Email: bernard@eng.umd.edu

Athanassios A. Dimas and Isaac Lottati
Krispin Technologies, Inc.
1370 Piccard Dr., Rockville, Maryland 20850 / Email: adimas@krispintech.com

ABSTRACT

This paper describes our recent efforts in developing a vortex method suitable for turbulent flow prediction. In this approach, vortex tubes are used as the principal computational element. They are supplemented adjacent to solid boundaries by an unstructured array of triangular vortex sheet prisms in several layers. The tubes are meant to model actual flow features; the sheets provide enhanced efficiency in resolving the turbulent viscous sublayer. A fully adaptive, parallel implementation of the Fast Multipole Method is used to determine velocities. Following a discussion of some of the principal features of the method, we present preliminary results of computations of several complex engineering flows.

1 INTRODUCTION

A primary motivation for the introduction of vortex methods almost three decades ago [1,2] was the belief that they should have unique advantages for the simulation and modeling of turbulent flows at high Reynolds number. In particular, unlike methods which use either a diffusive subgrid model or numerical diffusion to model turbulence as an equivalent, low and variable Ryenolds number flow, they can potentially represent the full range of high Reynolds number physics.

Subsequent development of the methodology revealed that successful application of vortex methods to complex, high Reynolds number, three-dimensional engineering flows depends critically on their resolution and speed. A "reasonable" accounting of small scales is necessary to fairly model turbulence, and an efficient solution to the difficult N-body problem embedded in the Biot-Savart calculation of velocities must be found.

Only relatively recently has the development of adaptive, parallel versions of the fast multipole method (FMM) [3,4,5] opened up the door to the kind of resolution needed to treat engineering flows. Less certain has been how to orchestrate a 3D turbulent flow calculation using vortex elements which both adheres to the physics of turbulence yet limits the numbers of vortex elements to the point where with the help of the parallel FMM, practical turbulent flow predictions can be made.

This paper will describe a vortex method which has been specifically designed to achieve these ends. It is meant for turbulent flow predictions and we hope it may be regarded as a useful alternative to traditional Reynolds-Averaged Navier-Stokes (RANS) and grid-based LES models. In this approach vortex tubes are used to represent the vorticity field everywhere except close to the boundary, where a fixed, thin, unstructured triangular mesh of finite thickness vortex sheets is used. The sheets are stacked normal to the surface several layers deep, with a half-thickness sheet adjacent to the boundary, and are meant to cover the viscous sublayer of turbulent wall flows.

After a description of the methodology we present examples from a number of recent calculations showing the effectiveness of the approach. These include calculations of an engine intake flow, the flow past a prolate spheroid and a minivan. The latter two calculations have been made using the VORCAT^{TM} code, which has been developed through U.S. Department of Energy sponsorship. This represents a commercial implementation of the scheme designed for general engineering applications (see www.krispintech.com).

2 THE VORTEX METHOD

2.1 Vortex tube elements

To reasonably well represent the dynamics of turbulent flow, a vortex method needs to resolve the energy containing scales of turbulence down to, perhaps, the inertial range, as well as the dynamical processes leading to the generation of new coherent vortices near boundaries. In both these instances it can be expected that tube-like vortical elements are a realistic model for the actual structure found in flows. For this reason there is likely to be advantage in utilizing vortex filaments as the primary computational element in the numerical scheme. The vortex tubes are composed of a number of straight-line segments, or "vortons." Note that we impart a quasi-physical significance to our vortex tubes, i.e. we do not view them as purely computational elements. From this perspective, the small scale structures of turbulent flow do not generally need multiple vortex elements for their representation. This is one means for making more effective use of vortices in the calculation.

As described at length by Chorin [6], a field of vortex tubes tend to stretch and fold while bringing energy to dissipation scales. Such natural adaptivity is a real physical effect in turbulence, but it is one which must be controlled lest vast numbers of vortex elements appear to describe the dynamics of the dissipation process in excruciating detail. An effective solution to this problem was pioneered by Chorin [7]: remove small scale hairpin shapes that form in the course of the folding process, as shown in Fig. 1. The rationale for hairpin removal is that the velocity field associated with hairpins is mostly local. Moreover, further calculation of the hairpin will only track the movement of the localized energy to dissipation scales. Thus, rather than invest in computing the small scale folding process, a simple estimate of the energy loss can be achieved by merely cutting away the hairpin and reattaching the ends of the tube. The smallest resolvable scale is determined by the minimum length of the vortex segments composing a filament. This can be adjusted depending on many criteria ranging from physical to computational considerations. Clearly, the smaller the allowed resolution, the more accurate the model.

The dynamics of the vortex tubes are governed by the 3D vorticity equation

$$\underbrace{\frac{\partial \mathbf{\Omega}}{\partial t} + (\nabla \mathbf{\Omega})\mathbf{u} = (\nabla \mathbf{u})\mathbf{\Omega}}_{convect\ filament\ endpoints} + \underbrace{\frac{1}{R_e}\nabla^2 \mathbf{\Omega}}_{decay\ model} , \qquad (1)$$

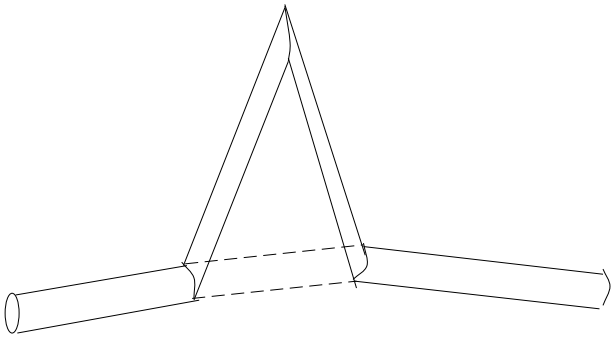

Figure 1. Hairpin removal via Chorin's algorithm.

where $\mathbf{u}$ is the velocity, $\mathbf{\Omega}$ is the vorticity and R_e is the Reynolds number. This is solved as indicated: convection, vortex stretching and reorientation are accommodated by moving the end points of the vortons. As they lengthen, they are divided into smaller segments. A decay model, described in the next section, is used to account for long time diffusive effects on the vortex tubes. In particular, we may assume that viscous dissipation plays some role in the demise of coherent vortices in a turbulent flow. This is especially a concern in internal flows, such as periodic channel flow, where vortices, once present, will persist indefinitely unless steps are taken to model their aging process. In contrast, for external flows, viscous decay of vortices can be assumed to take place downstream of the region of interest and hence is of less of a concern. Apart from the decay model, Eq. (1) is a standard approach for filament calculations [7, 8].

2.2 Vortex tube creation and destruction

Two different models of the vortex destruction process have been developed in order to help restrict vortices to those which are most dynamically important. The intent is also to mimic the finite lifespan of coherent vortices in real turbulent flow. Future research will look into optimal ways for accommodating the destruction process, though it should be noted – as suggested above – that this is not a great concern for external flows.

Preliminary calculations of channel flow [9] have shown that long lived vortices often have many segments, and tend to be without favored orientation. In this state it is safe to imagine that a vortex is "dissipated" and may be removed from the calculation without undue harm. In practical terms this proves to be an effective means for preventing runaway growth in the number of vortices.

An alternative approach is to consider the accumulated effect of vortex stretching versus viscous spreading on each individual tube. The well known

Gaussian core solution [2] establishes an equilibrium radius for tubes, r_e, in which vortex stretching is in equilibrium with diffusion. For a tube whose length increases from Δs to $\Delta s'$ in time Δt it may be shown that

$$r_e = 2\sqrt{\frac{\Delta t}{R_e(\Delta s'/\Delta s - 1)}}. \tag{2}$$

Generally, the radius of a vortex is either above or below the value of r_e associated with local stretching. If $r > r_e$, the vortex tends to get thinner, if $r < r_e$, it tends to widen. While it may be possible to model the process by which vortices change core size [10], such an approach is unsuited to the present purposes, since it fails to provide for retiring of old structures. The latter objective can be fulfilled, however, by providing for loss of circulation from the tubes whenever $r < r_e$. The amount is determined by the extent to which vorticity would diffuse beyond r due to the imbalance of vortex stretching and diffusion. The necessary relation is

$$\Gamma^{n+1} = \Gamma^n \left(1 - \frac{4\Delta t}{R_e}\left(\frac{1}{r^2} - \frac{1}{r_e^2}\right)\right), \tag{3}$$

where Γ^n is the circulation at time n. If $r > r_e$, the circulation may be left the same, i.e.

$$\Gamma^{n+1} = \Gamma^n, \tag{4}$$

and if the tube faces a net contraction, i.e. $\Delta s' < \Delta s$, then the maximum circulation loss can be assessed, namely

$$\Gamma^{n+1} = \Gamma^n \left(1 - \frac{4\Delta t}{R_e}\frac{1}{r^2}\right). \tag{5}$$

For tubes composed of multiple segments, the average of Δs and $\Delta s'$ over all segments can be used.

As the scheme is presently constituted, the same radius is given to all vortices. Since high shear near the walls leads to high stretching rates and hence small r_e, the influence of (3) or (5) in reducing Γ should be most pronounced away from the wall where vortices are less organized and experience slower rates of stretching. Whenever the circulation of a vortex drops below a threshold, it is dropped from the calculation, thus providing a second means for eliminating vortices.

Providing for each new generation of vortices as they are produced in a turbulent flow is also a critical aspect of the numerical scheme. The algorithm must at the same time be both sensitive to the physical process by which new structures appear, yet not so unconstrained as to allow for the formation of impossibly large numbers of new vortices. One means for accommodating these conditions has been previously developed [9, 11] and has been adapted for use in VORCAT. In this, vorticity arriving at the outer sheet layer is formed into new tubes whenever it surpasses a threshold. This will happen in regions of significant turbulence ejection and where the flow is separating. To further restrict the number of vortons, new ones are allowed to acquire vorticity over several consecutive time steps until they have convected away from their initial location.

2.3 Vortex sheet elements

Once vorticity is generated on solid surfaces, its evolution within the vortex sheet mesh is followed by solving the vorticity equation in conservative form:

$$\frac{\partial \mathbf{\Omega}}{\partial t} = \nabla \times \mathbf{F} + \frac{1}{R_e}\nabla^2 \mathbf{\Omega}, \tag{6}$$

where $\mathbf{F} = \mathbf{u} \times \mathbf{\Omega}$. An explicit forward scheme is used for the temporal discretization and an unstructured, finite-volume, upwind scheme for the spatial discretization on the right-hand side of (6).

The derivatives of $\mathbf{F}$ at grid points are computed using the divergence theorem,

$$\frac{\partial F_i}{\partial x_j} = \frac{1}{V}\int_S F_i n_j \, dS, \tag{7}$$

where V is the volume of the surrounding prisms and S is their bounding surface. An upwind scheme is used for the flux computation on the surface. The surface of each prismatic volume consists of several triangular or quadrilateral areas. Each of these is bounded by two triangular prisms: the "R" prism is the one towards which the surface unit normal vector, $\mathbf{n}$, is directed, while the other is denoted as the "L" prism. For every surface, the value of F_i is chosen based on the value of the normal component of the velocity field, i.e., the projection along vector $\mathbf{n}$. To this purpose, u_R is defined as the normal component of the velocity at the centroid of the "R" prism, while u_L is defined at the centroid of the "L" prism. Then, the appropriate F_i value is chosen based on the following criterion:

$$F_i = \begin{cases} F_i^L \text{ if } u_L \geq 0 \text{ and } u_L + u_R \geq 0 \\ F_i^C \text{ if } u_L < 0 \text{ and } u_R > 0 \\ F_i^R \text{ otherwise} \end{cases} \tag{8}$$

where F_i^R is the value of F_i at the centroid of prism "R", F_i^C is the value of F_i at the surface itself, and F_i^L is the value of F_i at the centroid of prism "L".

A similar approach may be used for the diffusion term, although for high Reynolds number flows only the wall normal diffusion term is retained and is computed by a finite-difference scheme.

3 VELOCITY FIELD

In a vortex method the velocity field is recovered from the vorticity field via

$$\mathbf{u}(\mathbf{x},t) = \int_{\Re^3} K(\mathbf{x}-\mathbf{x}')\mathbf{\Omega}(\mathbf{x}',t)d\mathbf{x}' + \mathbf{u}_p(\mathbf{x},t), \quad (9)$$

where

$$K(x,y,z) = -\frac{1}{4\pi \mid \mathbf{x} \mid^3}\begin{pmatrix} 0 & -z & y \\ z & 0 & -x \\ -y & x & 0 \end{pmatrix}, \quad (10)$$

is the Biot-Savart kernel and $\mathbf{u}_p$ is a potential flow added to enforce the non-penetration boundary condition at solid surfaces. Following standard practice [7,8], that part of the integral in (9) due to the ith vorton is approximated via

$$\int_{\Re^3} K(\mathbf{x}-\mathbf{x}')\mathbf{\Omega}(\mathbf{x}',t)d\mathbf{x}' \approx -\frac{\Gamma_i}{4\pi}\frac{\mathbf{r}_i \times \mathbf{s}_i}{\mid \mathbf{r}_i \mid^3}\,\phi(r/\sigma) \quad (11)$$

where

$$\phi(r) = \left(1 - \left(1 - \frac{3}{2}r^3\right)\right)e^{-r^3}$$

is a high-order smoothing function, Γ_i is the circulation, $\mathbf{r}_i = \mathbf{x} - \mathbf{x}_i$, $\mathbf{s}_i$ is an axial vector along the length of the tube and σ is a smoothing parameter.

To evaluate the contribution to the velocity from the triangular-prism sheets, we take advantage of their being thin to convert the volume integral in (9) to an area integral times the sheet thickness. For enhanced accuracy the vorticity field is taken to be piecewise linear over the triangles. In this case, analytic evaluation of the integral in Eq. (9) is done where possible, and where not, it is evaluated numerically using Simpson's rule. Note that after integration $K(\mathbf{x}-\mathbf{x}_i)$ is for the most part desingularized, though in some cases, particularly near the edge of triangles, a finite velocity is only the end result of a cancelation of singular terms. These special cases are handled in the code by forcing analytic cancelation.

The potential flow necessary to ensure non-penetration is derived from a collection of source panels covering the same unstructured triangular surface mesh as used in computing the sheet vorticity field. A piecewise linear distribution of the source strength field, q, is assumed. q is determined from numerical solution of the defining equation

$$\frac{1}{4\pi}\int_S \frac{q(\mathbf{n}\cdot\mathbf{r})}{r^3}dS' = -\mathbf{n}\cdot\mathbf{u}_\mathbf{v} \quad (12)$$

where $\mathbf{r} = \mathbf{x} - \mathbf{x}'$. The left-hand side is the surface normal velocity induced on the surface point $\mathbf{x}$ by q and the right-hand side is the opposite of the surface normal velocity induced by the vortex elements. By enforcing Eq. (12) at the node points of the triangularized surface, a linear system of equations for nodal point source strengths results, namely,

$$A_{ij}q_j = -\mathbf{n}\cdot\mathbf{u}_{\mathbf{v_i}} \quad (13)$$

where each element of A_{ij} is the normal velocity induced at surface node point i by a piecewise linear source distribution with unit strength at node point j and zero elsewhere. The matrix A_{ij} is computed in the precomputation stage of the code and need not be repeated. At each time step the right-hand side of Eq. (13) changes and a new set of values for q_i must be determined.

The evaluation of $\mathbf{u}_p$ from the source panels involves integrals identical to those appearing in Eq. (9), so the same integral evaluations can be used for both purposes.

For those vortons lying within the sheet region adjacent to the boundary, the velocity is found using three-dimensional linear interpolation over the nodal points of the triangular prisms. This is found to enhance the accuracy of vorton motions and most importantly prevent the passage of vortons into solid bodies.

Vorticity in the half-thickness vortex sheets touching solid surfaces is determined by enforcing the non-slip boundary condition via finite difference approximation to their definition in terms of velocities. The vorticity in the wall half-sheets does not contribute to the velocity elsewhere in the flow since they are imagined to be matched with half-thickness image vortex sheets which exactly cancel their induced wall-normal velocity at the boundary surface. In other words, a wall sheet and its image induce a velocity tangential to the wall in the region between them: one which balances the velocity due to all other sheets and vortons.

Outside the region between the sheets, their contribution to velocities exactly cancel [12].

4 FAST MULTIPOLE METHOD

A fully adaptive, parallel implementation of the FMM has been developed and is now part of the VORCAT code. In the adaptive FMM, the domain is partitioned into nested cubic boxes such that no box has more than a predetermined number of vortons. Regions with a high concentration of vortons are covered by many small boxes, whereas, regions with few vortons have a small number of large boxes. The partitioning results in an oct-tree structure with the computational domain at the root of the tree, and the shape of the tree determined by the distribution of the vortons. The tree structure provides the hierarchy necessary to achieve an operation count of $O(N_v \log N_v)$ instead of the nominal $O(N_v^2)$ for N_v vortons.

Efficiency in the FMM is gained by combining the vector potential induced by vortons in the root boxes into truncated expansions in spherical harmonics about the centers of the boxes. These expansions are combined into expansions over parent boxes at higher levels in the tree. Expansions at the highest level are then shifted down a separate tree of field points formed from boxes containing the points where the velocity needs to be evaluated. The cumulative effect of many vortons is thus brought down to the evaluation of a single expansion at the root level of the field tree. Precautions have to be taken to make sure that vortons in adjacent boxes contribute to each others' velocity outside of the multipole expansions, in order to preserve the accuracy of the computation. This adaptive fast multipole method is based on the algorithm of Strickland and Baty [4].

Parallelization of the adaptive FMM was helped by assuming that computational costs far exceeds memory requirements even for $O(10^7)$ vortons. Consequently, each processor was given its own copy of the tree, and even though each processor does not need the source expansion coefficients for every node in the tree, a total exchange of coefficients in the source expansion was done anyway. These assumptions make it significantly easier to parallelize the adaptive FMM algorithm.

The parallel algorithm follows the Bulk Synchronous Parallel (BSP) model for scalable computing [13]. BSP is a parallel programming model for designing efficient, portable, and predictable scalable code. A BSP computation consists of a sequence of parallel supersteps. Each superstep consists of computations on values held locally plus any necessary communications followed by a barrier synchronization. After the barrier, any remote memory accesses are guaranteed to have taken effect.

The adaptive FMM computation has 2 supersteps: one for the source expansions, and one for the field expansions and velocities. The tree is partitioned in such a way that the resulting sub-trees have, as close as possible, the same number of points. These sub-trees are used to distribute the work in the 2 supersteps. Details of the algorithm including timings on an Origin 2000 have been reported by Collins, et al. [5].

5 RESULTS

The capability of VORCAT in predicting turbulent flow is currently being assessed. The validation process takes many directions including applying VORCAT to the prediction of a variety of well documented turbulent flows. Included in this is an exploration of its sensitivity to parameters such as σ, maximum vorton length, hairpin removal angle, vorton creation threshold, sheet density and thickness, number of sheet levels as well as parameters associated with the decay model, the FMM and other aspects of the velocity computation. We concentrate here on presenting preliminary results from three recent applications of VORCAT. The first is a calculation showing the interaction between flow entering an idling aircraft engine and the ground plane. This was done with a prototype of VORCAT. The second two applications study the flow past a 6:1 prolate spheroid at angle of attack and a minivan. Each of these were computed using the most recent, fully adaptive, VORCAT code.

5.1 Engine intake flow

The airflow between the ground and the intake of a stationary or taxiing aircraft jet engine at high thrust levels, may lead to strong vorticity generation [14]. In this, small vortices generated on the ground are drawn into the engine inlet. Under conditions which are not well understood, the stream of rotational fluid strengthens to form discernible vortical structures extending from the ground up to the engine. Such vortices are a potential hazard since they can create suction forces strong enough to disrupt the flow ahead of the compressor blades possibly causing compressor stall, or even pick up foreign objects from the runway and inject them into the engine.

Current RANS solvers cannot correctly predict vorticity generation by the separated ground flow induced by suction of the aircraft engine. To investigate the capabilities of VORCAT in this complex

flow, we considered an idealized problem wherein the jet engine is modeled as a cylinder with the same length/diameter and height/diameter ratios (3 and 1.5, respectively) as an actual engine for which this phenomenon is known to occur. Pictures of the vorton distribution for the case with a cross-wind at 5% of the engine intake velocity and $R_e = 5,000,000$ are shown in the sequence of front views in Figs. 2 - 7 in intervals of 22 time units since impulsive startup of the engine. It is seen that vortices generated on the ground are drawn into the engine intake. With time, these strengthen and appear to combine into several substantial vortices. A sideview at the last time step is given in Fig. 8 and a top view in Fig. 9. It is interesting to note the tendency for larger scale vortical structures to form throughout the turbulent boundary layer on the ground plane. We also see that the effect of the crosswind is to blow the intake vortices to the side; in other calculations without crosswind, illustrated through the streamline plot in Fig. 10, the intake flow is centrally aligned. This flow differs markedly from the equivalent potential flow. Future calculations will take into account swirl in the engine intake plane.

5.2 Prolate spheroid

The flow past a 6:1 prolate spheroid under a variety of conditions has been the object of considerable attention in physical experiments [15,16] and thus provides a convenient venue with which to examine the effectiveness of our vortex method in predicting high Reynolds number flows. In the case studied here, the Reynolds number based on free stream velocity and axial length is $R_e = 4,200,000$. The spheroid has 4752 triangles covering its surface and there are 6 sheet levels, each of thickness 0.0017. Figs. 11 - 13 show the vorton distribution from the side, front and back, respectively, at approximately $t = 1.5$ (1500 time steps) after impulsive startup. There are approximately 200,000 vortons in the image, and it should be noted there is also considerable vorticity (not depicted) in the vortex sheets adjacent to the surface.

The figure shows massive separation off the surface in the form of a rolled up vortex. Pressure contours, computed using the integral formulation of Uhlman [17] and shown in Fig. 14, also reflect this behavior. From the pressure and surface vorticity, estimates of the drag and lift forces have been made. For the time step shown in the figure, the drag and lift coefficients are, respectively, $C_D = 1.06$ and $C_L = .53$, values well within the range predicted in physical experiments [15,16], which run from $0.9 - 1.2$ for C_D. The force coefficients in the axial (x) and normal (y) directions are $P_x = 0.64$, $P_y = 0.98$ for the pressure and $V_x = 0.01$ and $V_y = 0.01$ for the viscous forces. When the forces are calculated over a period of time they show a distinct periodicity suggesting that alternate shedding of the large vortex is likely to occur. Further extension of the current calculations in time hope to verify the occurrence of this behavior.

5.3 Minivan

The minivan which is being investigated is depicted in Fig. 15 in the form of the surface mesh triangularization used by VORCAT. In this study there is no ground plane. The computed vorton distribution at approximately $t = 2$ after impulsive start is shown in Fig. 16. At this time a prominent feature of the wake flow is a single large vortex. Symmetry breaking was not forced in the calculation: evidently, rotation of the opposite sign is possible depending on the particular details of the simulation. On the side shown in the figure, the flow separates off the hatch back of the van and curls up into the large wake vortex. Note the system of parallel vortices formed on the side in the direction of flow. This study is ongoing and will be extended in the future to include comprehensive force predictions, the addition of a ground plane and other changes in boundary conditions.

6 CONCLUSION

The vortex method for turbulent flow simulation described herein has made a promising start toward achieving the capability of efficiently modeling complex, high Reynolds number turbulent flows. Reasonable force and pressure predictions have been made; flow and wake structure developing on the prolate spheroid and minivan show many realistic features. Furthermore, the method has been demonstrated to have some capability for modeling the difficult engine intake flow. Further work will investigate the sensitivity of the approach to the various simplifications used in creating an efficient scheme, and attempt to demonstrate a close connection between the modeled and experimental predictions for both the flows presented here as well as a range of other important flows.

ACKNOWLEDGMENT

This work was supported by the Department of Energy under SBIR Award No. DE-FG02-97ER82413 and resulted in a software package that is pending a US patent. Computer time on the Origin2000 was provided by the CFD Group of SGI, Eagan, Minnesota.

REFERENCES

[1] Chorin, A. J. (1973), "Numerical study of slightly viscous flow," J. Fluid Mechanics, Vol. 57, p. 785 - 796.

[2] Leonard, A. (1975), "Numerical simulation of interacting, three-dimensional vortex filaments. *Lec. Notes in Phys.*, Vol. 35, p. 245 - 250.

[3] Greengard, L. and Rokhlin, V. (1987), "A fast algorithm for particle simulations," J. Comput. Phys., Vol. 73, p. 325-348.

[4] Strickland, J. H. and Baty, R. S. (1993), "A three dimensional fast solver for arbitrary vorton distributions," *Technical Report SAND93-1641*, Sandia National Laboratories.

[5] Collins, J. P., Dimas, A., and Bernard, P. S. (1999), "A parallel adaptive fast multipole method for high performance vortex method based simulations," Proc. ASME IMECE'99, Nashville, Tenn.

[6] Chorin, A. J. (1982), "The evolution of a turbulent vortex," Comm. Math. Physics, Vol. 83, p. 517 - 535.

[7] Chorin, A. J. (1993), "Hairpin removal in vortex interactions II," J. Comput. Phys., Vol. 107, p. 1-9.

[8] Puckett, E. G. (1993), "Vortex methods: an introduction and survey of selected research topics," in *Incompressible Computational Fluid Dynamics: Trends and Advances*, M. D. Gunzburger and R. A. Nicolaides, ed., Cambridge University Press, p. 335-407.

[9] Bernard, P. S. (1999), "Toward a Vortex Method Simulation of Non-Equilibrium Turbulent Flows," in *Modeling Complex Turbulent Flows*, M.D. Salas et al., Kluwer Academic Pub., p. 161 - 181.

[10] Rossi, L. (1995), "Resurrecting core spreading vortex methods: a new scheme that is both deterministic and convergent," SIAM J. Sci. Comp., Vol. 17, p. 370.

[11] Bernard, P. S., A. Dimas, and P. Collins, (1999), "Turbulent flow modeling using a fast, parallel, vortex tube and sheet method," *ESAIM Proceedings, Third International Workshop on Vortex Flow and Related Numerical Methods*, Vol. 7 Sept 1999 Editors: A. Giovannini, et al. http://www.emath.fr/Maths/Proc/Vol.7/index.html, p. 46 - 55.

[12] Bernard, P. S. (1995), "A deterministic vortex sheet method for boundary layer flow," J. Comput. Phys., Vol. 117, p. 132-145.

[13] McColl, W. F (1995), "Scalable computing," *Lecture Notes in Computer Science*, Vol. 1000, p. 8, Springer-Verlag.

[14] Campbell, J. F. and Chambers, J. R. (1994) "Patterns in the sky: natural visualization of aircraft flow fields," NASA SP-514.

[15] Chesnakas, C. J., and Simpson, R. L. (1994) "Full three-dimensional measurements of the cross-flow separation region of a 6:1 prolate spheroid," Experiments in Fluids, Vol. 17, p. 68-74.

[16] Wetzel, T. G., Simpson, R. L. and Chesnakas, C. J. (1998), "Measurement of three- dimensional crossflow separation," AIAA Journal, Vol. 36, p. 557-564.

[17] Uhlman Jr., J. S. (1992), "An integral equation formulation of the equations of motion of an incompressible fluid," NUWC-NPT Technical Report 10,086, Naval Undersea Warfare Center Division, Newport, Rhode Island.

Figure 2. Front view of engine flow at t=33.

Figure 3. Front view of engine flow at t=55.

Figure 4. Front view of engine flow at t=77.

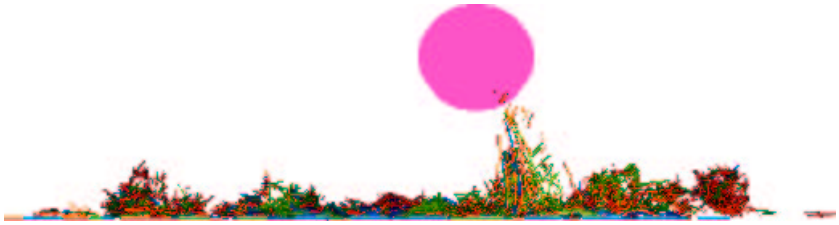

Figure 5. Front view of engine flow at t=99.

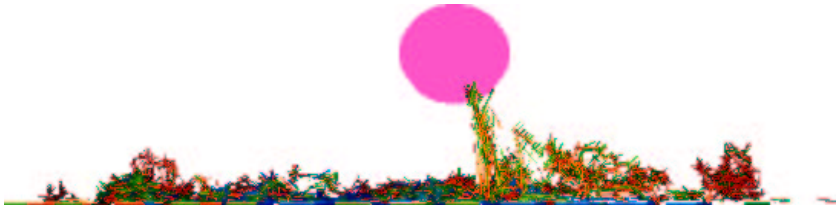

Figure 6. Front view of engine flow at t=121.

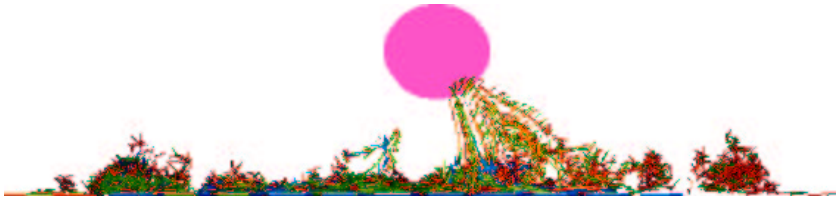

Figure 7. Front view of engine flow at t=143.

Figure 8. Side view of engine flow at t=143.

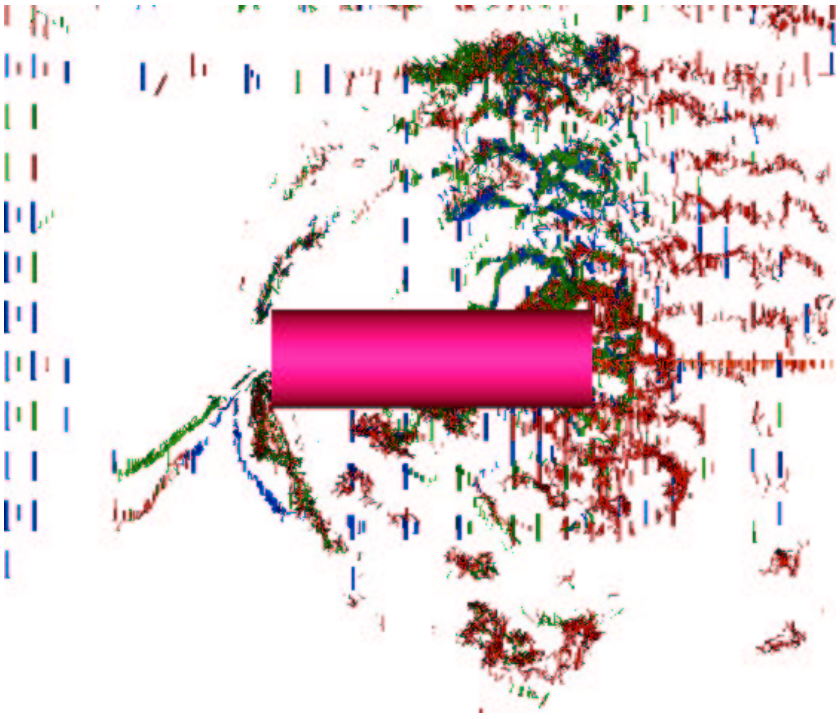

Figure 9. Top view of engine flow at t=143.

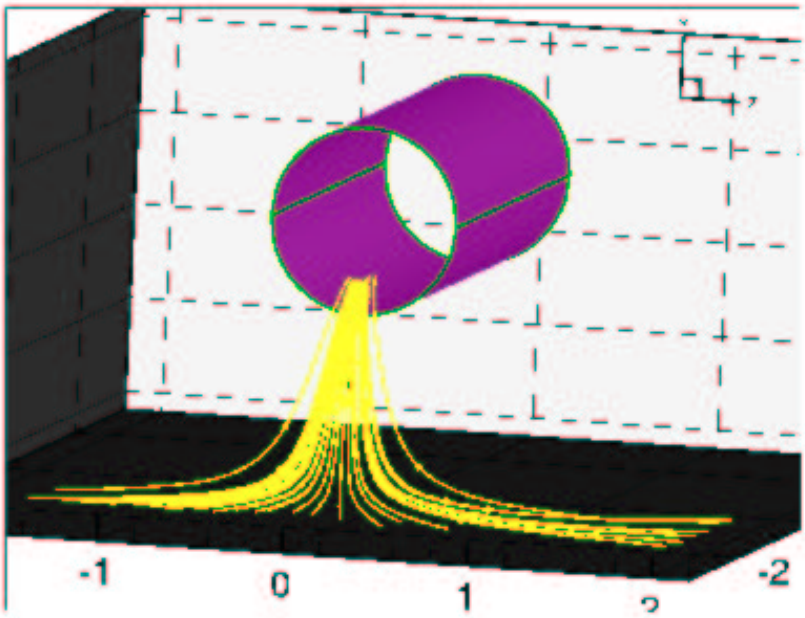

Figure 10. Streamlines without cross flow.

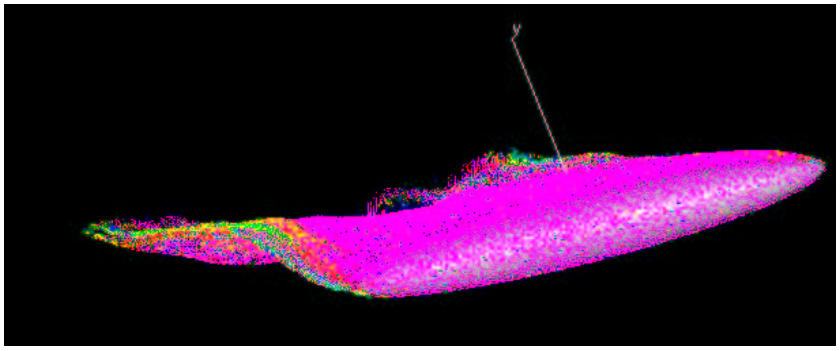

Figure 11. Side view of prolate spheroid at 30° angle of attack.

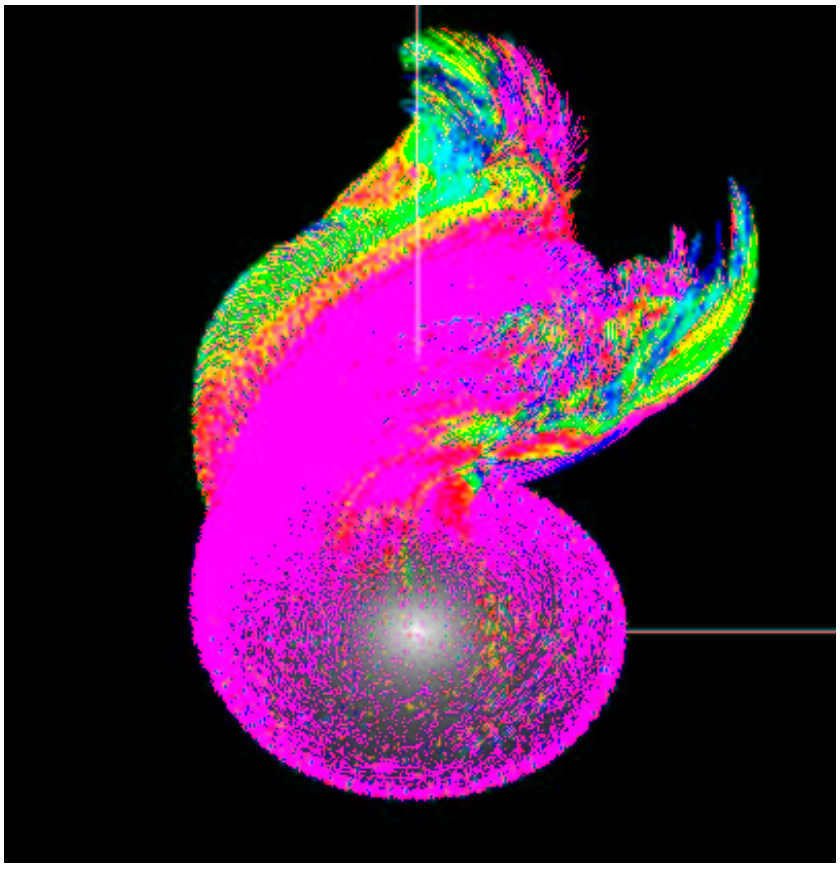

Figure 12. Front view of prolate spheroid at 30° angle of attack.

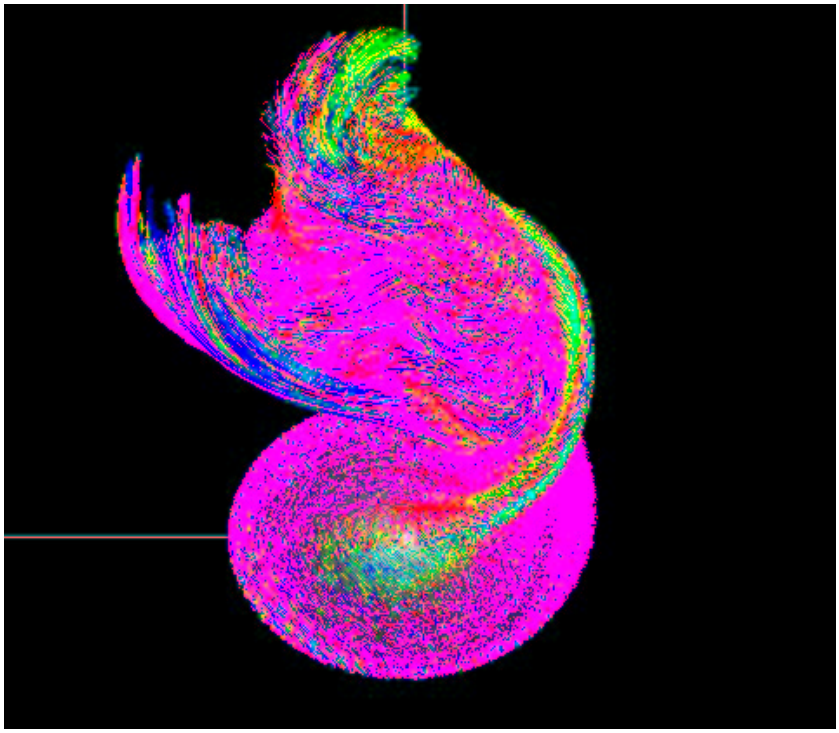

Figure 13. Rear view of prolate spheroid at 30° angle of attack.

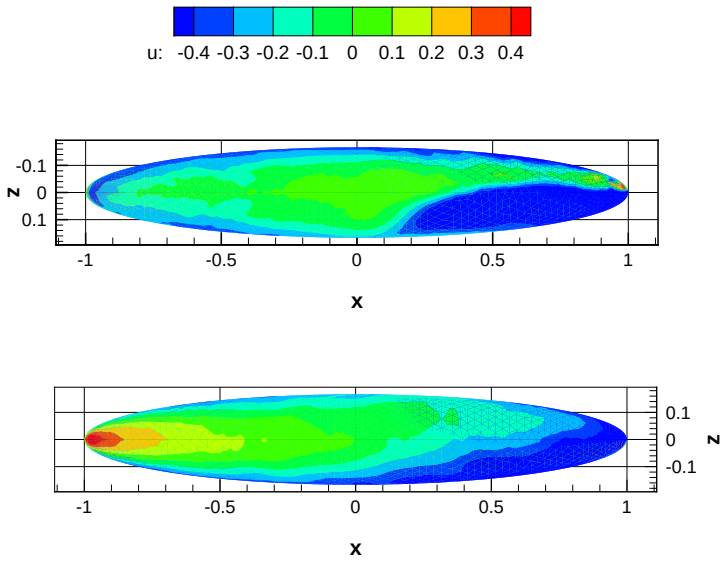

Figure 14. Pressure contours, top and bottom view.

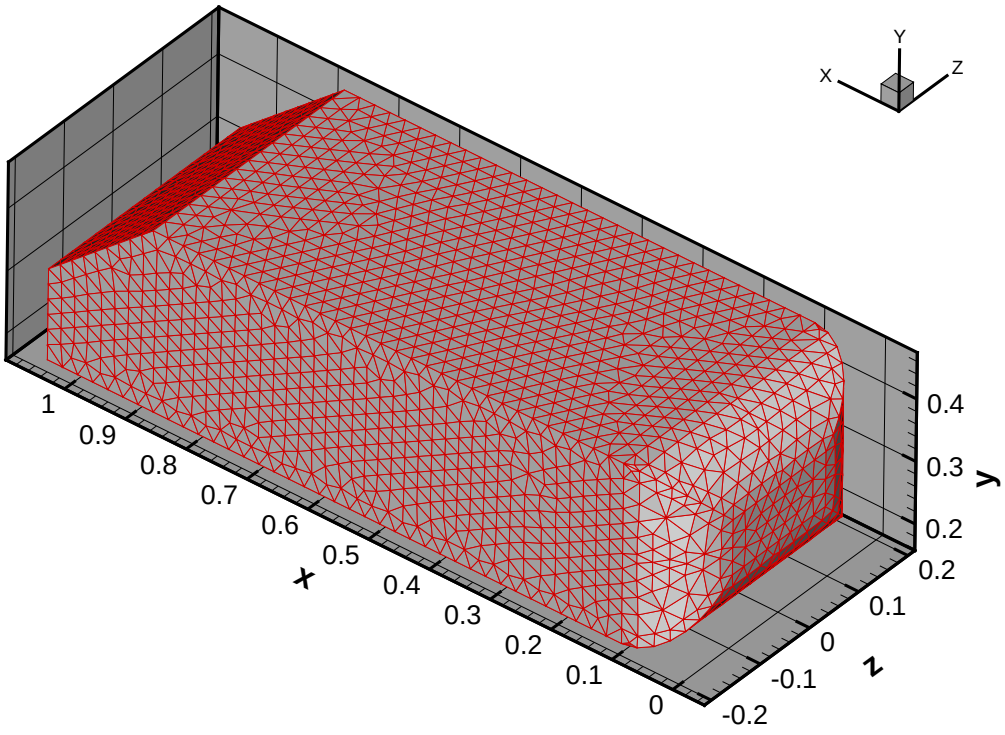

Figure 15. Minivan sheet mesh.

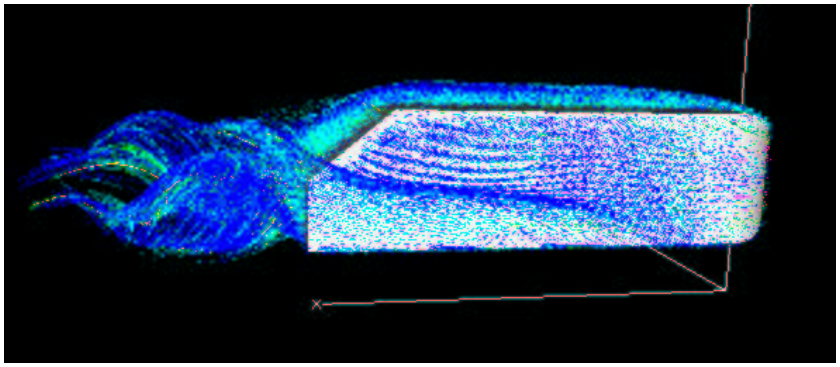

Figure 16. Minivan, side view.